

# Many-Body Quantum Muon Effects and Quadrupolar Coupling in Solid Nitrogen

M. Gomilšek,<sup>1,2,3</sup> F. L. Pratt,<sup>4</sup> S. P. Cottrell,<sup>4</sup> S. J. Clark,<sup>3</sup> and T. Lancaster<sup>3</sup>

<sup>1</sup>*Jožef Stefan Institute, Jamova c. 39, SI-1000 Ljubljana, Slovenia*

<sup>2</sup>*Faculty of Mathematics and Physics, University of Ljubljana, Jadranska u. 19, SI-1000 Ljubljana, Slovenia*

<sup>3</sup>*Department of Physics, Durham University, South Road, Durham DH1 3LE, United Kingdom*

<sup>4</sup>*ISIS Muon Group, Science and Technology Facilities Council (STFC), Didcot OX11 0QX, United Kingdom*

(Dated: February 15, 2022)

Quantum zero-point motion (ZPM) of light particles in materials has only recently begun to be explored from an *ab initio* perspective, through several competing approximations. Here we develop a unified description of muon (or light nucleus) ZPM and establish the regimes of anharmonicity and positional quantum entanglement where different approximation schemes apply. Via density functional theory and path-integral molecular dynamics simulations we demonstrate that in solid nitrogen,  $\alpha$ -N<sub>2</sub>, muon ZPM is both strongly anharmonic and many-body in character, with the muon forming an extended electric-dipole polaron around a central, quantum-entangled [N<sub>2</sub>- $\mu$ -N<sub>2</sub>]<sup>+</sup> complex. By combining this quantitative description of quantum muon ZPM with precision muon quadrupolar level-crossing resonance experiments, we independently determine the static <sup>14</sup>N nuclear quadrupolar coupling constant of pristine  $\alpha$ -N<sub>2</sub> to be  $-5.36(2)$  MHz, a significant improvement in accuracy over the previously-accepted value of  $-5.39(5)$  MHz.

Quantum zero-point motion (ZPM) of nuclei plays an important role in the structure and dynamics of materials, especially those containing light atoms such as hydrogen [1–3]. ZPM should be even more pronounced for implanted muons  $\mu^+$ , which act as sensitive probes in muon spin relaxation ( $\mu$ SR) experiments [4–6], since a muon has just 1/9 of the proton mass. We expect a large muon zero-point energy  $ZPE \propto m_\mu^{-1/2} \sim 0.7$  eV [5, 7–11], corresponding ZPM delocalization  $\Delta x \propto m_\mu^{-1/4} \sim 0.2$  Å around isolated muon stopping sites, the merging of candidate muon sites separated by low energy barriers, quantum tunneling, diffusion, and even muon Bloch waves [12, 13]. Beyond these, many-body quantum effects like positional entanglement between muons and nuclei are also expected. Muon ZPM challenges the approach of predicting muon stopping sites and the lattice distortions around them using *ab initio* methods, often based on density functional theory (DFT) [7–9, 14], that treats the muon and nuclei as classical particles. Several schemes for approximating muon ZPM have been developed [8, 9], mainly divisible into: 1) adiabatic methods, based on a single-particle description [15–19], and 2) harmonic approximations [10, 20, 21]. Studies of quantum muons using computationally more demanding, but numerically-exact, path-integral molecular dynamics (PIMD) have remained rather sparse [1, 13, 22], despite its popularity in describing light-nuclei systems [1–3].

Here we develop a unified description of muon ZPM and the regimes in which particular approximations apply, via a DFT+PIMD study of muon ZPM in solid nitrogen,  $\alpha$ -N<sub>2</sub>. We characterize the regimes by the degree of (i) anharmonicity and (ii) muon–nuclear positional entanglement, the latter quantified with easy-to-calculate entanglement witnesses [23–25]. We find that in  $\alpha$ -N<sub>2</sub> anharmonic many-body quantum effects dominate, as anticipated from previous experimental [12] and theoret-

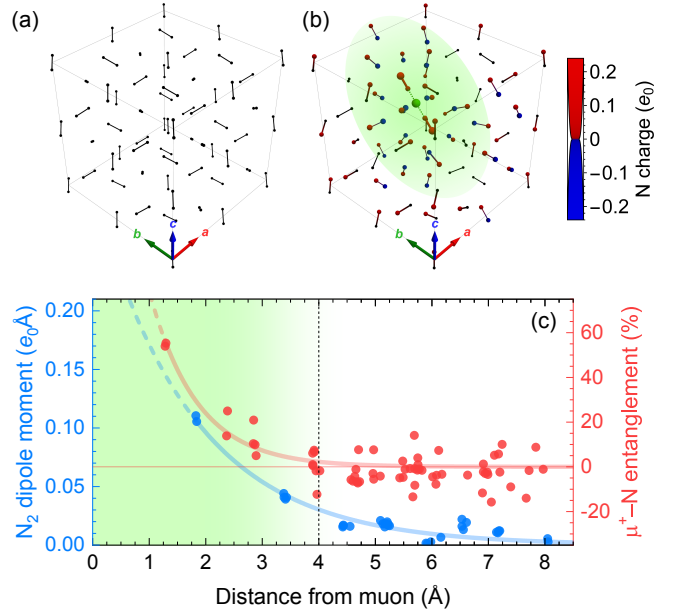


Figure 1. (a) Pristine  $\alpha$ -N<sub>2</sub>. (b) Classical  $\mu^+$  (green) in  $\alpha$ -N<sub>2</sub> induces an electric-dipole polaron (shading) around a linear [N<sub>2</sub>- $\mu$ -N<sub>2</sub>]<sup>+</sup> complex. Sphere size/color gives the induced DFT Mulliken charge of nitrogen ions. (c) Induced N<sub>2</sub> electric dipole moments (blue) and degree of muon–nuclear positional entanglement  $c$  from PIMD (red). Solid lines are exponential fits, dashed line/shading indicates the polaron size.

ical work [26], and discover that an extended electric-dipole polaron of polarized N<sub>2</sub> molecules forms around a central [N<sub>2</sub>- $\mu$ -N<sub>2</sub>]<sup>+</sup> complex [Fig. 1(b)]. By applying these insights to our precision muon quadrupolar level-crossing resonance (QLCR) [27] experiments, we derive an independent estimate of the static nuclear quadrupolar coupling constant (NQCC) of <sup>14</sup>N with significantly improved accuracy compared to the literature value [28].

Within the classical, point-particle description of muons and nuclei using DFT, we find a single stable muon site at almost exactly the  $(0, 1/4, 1/4)$  position [Fig. 1(b)], which lies between two molecules of pristine  $\alpha$ -N<sub>2</sub> [29] but is not symmetric under its  $Pa\bar{3}$  space group [30, 31]. In line with *ab initio* simulations of muons [26] and protons [32–36] in N<sub>2</sub> clusters, we find that in crystalline  $\alpha$ -N<sub>2</sub> a muon forms an almost-linear, almost-centrosymmetric  $[\text{N}_2-\mu-\text{N}_2]^+$  covalent complex oriented along the  $[0, 1, 1]$  direction. Moreover, we find an unusual, extended electric-dipole polaron around this complex, where its positive charge induces electric dipole moments on nearby N<sub>2</sub> molecules [Fig. 1(c)], which causes them to reorient to point towards it. Up to  $\sim 4 \text{ \AA}$  from the muon, dipolar electrostatic interactions of polarized N<sub>2</sub> molecules with the  $[\text{N}_2-\mu-\text{N}_2]^+$  complex overwhelm the weak electric quadrupole and van der Waals (VdW) N<sub>2</sub>-N<sub>2</sub> interactions of pristine  $\alpha$ -N<sub>2</sub> [28, 37]. (This state is distinct from the small charge-neutral muon-polaron proposed in Cr<sub>2</sub>O<sub>3</sub> [38].)

To incorporate quantum effects we first employ single-particle, adiabatic approximations of muon–nuclear ZPM. Though elaborate schemes have been proposed [18, 19], the simplest are weakly- and strongly-bound muon approximations [15–17], corresponding to zero or maximal muon–nuclear entanglement, respectively. In both schemes, an effective single-particle muon potential  $V_{\text{eff}}(\delta\mathbf{x})$  is constructed from total DFT energy under muon displacements  $\delta\mathbf{x}$  from its classical site, while: (i) keeping the nuclei fixed at the positions corresponding to the unperturbed muon site (weakly-bound case), or (ii) letting them relax by  $\delta\tilde{\mathbf{r}}_N(\delta\mathbf{x})$  to new lowest-energy positions for each  $\delta\mathbf{x}$  (strongly-bound case) while keeping the center of mass fixed. Respectively, this corresponds to: (i) assuming independent muon and nuclear ZPM [i.e., a separable muon–nuclear wavefunction,  $\psi(\delta\mathbf{x}, \delta\mathbf{r}_N) = \psi_\mu(\delta\mathbf{x})\psi_N(\delta\mathbf{r}_N)$ ] in the weakly-bound case, or (ii) ZPM where a quantum measurement of the muon displacement  $\delta\mathbf{x}$  would simultaneously also determine all nuclear displacements  $\delta\mathbf{r}_N$  [i.e., a maximally-entangled muon–nuclear wavefunction,  $\psi(\delta\mathbf{x}, \delta\mathbf{r}_N) \propto \psi_\mu(\delta\mathbf{x})\delta(\delta\mathbf{r}_N - \delta\tilde{\mathbf{r}}_N(\delta\mathbf{x}))$ , where  $\delta$  is the Dirac delta function] in the strongly-bound case. Although, by the variational principle, the strongly-bound potential is shallower than the weakly-bound potential [Fig. 2(a,b)], the effective mass  $m_{\text{eff}}$  in the strongly-bound case increases above the free-muon mass  $m_\mu$  due to additional movement of nuclei with the muon, meaning that muon ZPM delocalization can increase or decrease in the strongly-bound case. Explicitly, assuming a linear dependence of the displacement of the  $i$ th nucleus of mass  $m_i$  on the muon displacement, i.e.,  $\delta\tilde{\mathbf{r}}_{N_i}(\delta\mathbf{x}) = A_i\delta\mathbf{x}$  where  $A_i$  is a tensor, the effective mass tensor in the strongly-bound case is given by  $m_{\text{eff}} = m_\mu\text{id} + \sum_i m_i A_i^T A_i$  where id is the identity. In the weakly-bound case  $m_{\text{eff}} = m_\mu$ . Once  $V_{\text{eff}}(\delta\mathbf{x})$  and  $m_{\text{eff}}$  are known, a single-particle

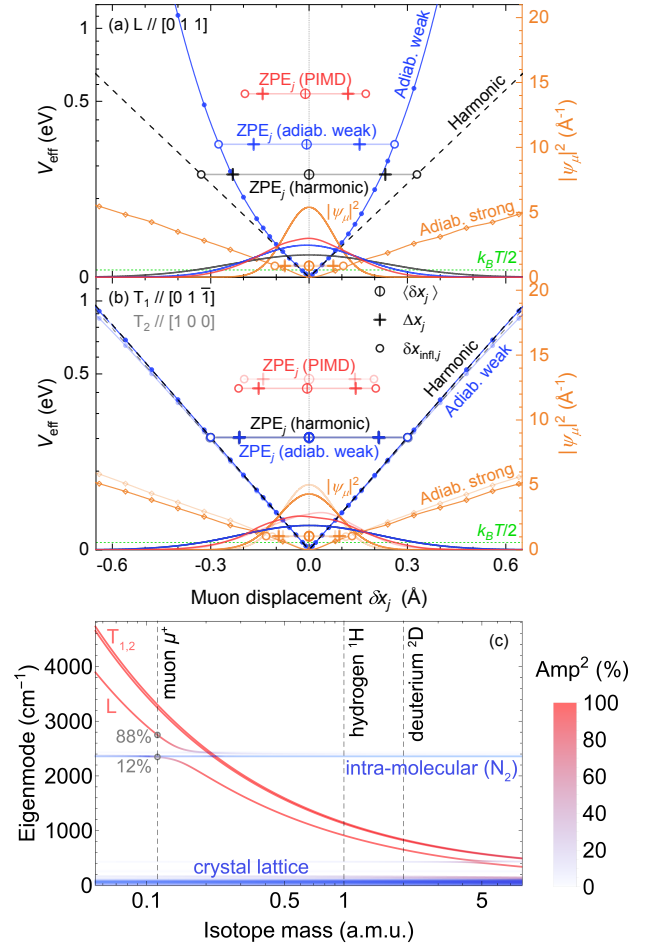


Figure 2. (a,b) Effective muon potential in a square-root-linear scale (harmonic potentials appear as straight lines) along the (a) L and (b)  $T_{1,2}$  directions for various approximations (left axis) with the corresponding ZPM muon probability density (right axis), directional contributions ZPE<sub>j</sub>, mean muon displacements  $\langle \delta x_j \rangle$ , wavefunction widths  $\Delta x_j$ , and inflection points  $\delta x_{\text{infl},j}$  where  $\partial^2 \psi_\mu / \partial (\delta x_j)^2 = 0$ . For PIMD ( $T = 20 \text{ K}$ ) ZPE<sub>j</sub> is estimated as the harmonic ZPE<sub>j</sub> yielding the same  $\Delta x_j$  if  $m_{\text{eff}} = m_\mu$ . (c)  $\Gamma$ -point phonon spectra of a supercell of muonated  $\alpha$ -N<sub>2</sub> vs. muon isotope mass  $m_\mu$  (plot generated from one DFT calculation [29]). Shading gives the muon amplitude squared in individual normal modes.

Schrödinger equation for the muon wavefunction  $\psi_\mu(\delta\mathbf{x})$ ,  $[-\hbar^2/(2m_{\text{eff}})]\nabla^2\psi_\mu + V_{\text{eff}}\psi_\mu = (ZPE)\psi_\mu$ , can be numerically solved to obtain the muon–nuclear ZPM and ZPE. This inherently single-particle approximation with 3 degrees of freedom in  $\delta\mathbf{x}$  (due to the assumed zero or maximal entanglement) cannot describe many-body ZPM involving more than 3 degrees of freedom (i.e., cases with partial muon–nuclear entanglement).

Fig. 2(a,b) shows the weakly- and strongly-bound adiabatic effective potentials. Separable potentials are assumed with an eigenaxis L  $\parallel [0, 1, 1]$  along the  $[\text{N}_2-\mu-\text{N}_2]^+$  complex and two,  $T_1 \parallel [0, 1, \bar{1}]$  and  $T_2 \parallel [0, 0, 1]$ , transverse, coinciding with muon  $\Gamma$ -point normal

mode directions from DFT [Fig. 2(c)]. In the weakly-bound case we find a total muon ZPE =  $\sum_j \text{ZPE}_j = 0.69 \text{ eV}$ , with directional contribution  $\text{ZPE}_j = 0.29 \text{ eV}$  and muon wavefunction width  $\Delta x_j = \langle \delta x_j^2 \rangle^{1/2} = 0.16 \text{ \AA}$  along the  $j = \text{L}$  direction, while  $\text{ZPE}_j = 0.20 \text{ eV}$  and  $\Delta x_j = 0.21 \text{ \AA}$  along  $j = \text{T}_{1,2}$ . Muon ZPM delocalization is thus significant compared to the  $1.29(1) \text{ \AA}$  distance between the classical muon site and the nearest nitrogen. However, in the strongly-bound case we also find large effective muon mass renormalization  $m_{\text{eff},j}/m_\mu = 810(160)$ ,  $350(40)$ , and  $520(80)$  along the  $j = \text{L}$ ,  $\text{T}_1$ , and  $\text{T}_2$  directions, respectively, due to electrostatic interactions within the polaron. These result in a reduced total ZPE =  $8.0(4) \text{ meV}$  with contributions  $\text{ZPE}_j = 2.1$ ,  $3.1$ , and  $2.8 \text{ meV}$  and ZPM delocalization  $\Delta x_j = 0.074(4)$ ,  $0.093(3)$ , and  $0.079(4) \text{ \AA}$  along these same directions.

Given the discrepancy between the two adiabatic approximations, one question is their applicability, i.e., whether muon–nuclear ZPM is minimally (weakly-bound limit), maximally (strongly-bound limit), or partially entangled. We address this using a toy model with the muon bound to nearby nuclei with force constants  $k_\mu$ , which are further bound to a static lattice with force constants  $k_n$ . If  $k_\mu \ll k_n$  muon displacements barely perturb the nuclei (weakly-bound limit), while if  $k_\mu \gg k_n$  muon displacements strongly displace nearby nuclei (strongly-bound limit). We estimate  $k_\mu/k_n$  in  $\alpha\text{-N}_2$  from the ratio of adiabatic potentials as  $k_\mu/k_n = V_{\text{eff}}^{\text{weak}}/V_{\text{eff}}^{\text{strong}} - 1 \approx 8\text{--}13$ , depending on direction [Fig. 2(a,b)]. This excludes the weakly- but not the strongly-bound adiabatic approximation. However, the relatively large  $k_\mu/k_n$  still competes with the tendency of light particles to partially decouple from the positions of heavier particles [12], which could lead to an intermediate, partially-entangled regime where single-particle (adiabatic) approximations fail.

An alternative class of approximations are harmonic methods [10, 20, 21], which work in the many-body regime of partial entanglement, but are limited to strictly harmonic muon–nuclear interactions. These start with a  $\Gamma$ -point DFT phonon calculation in the classical muon site geometry (a localized muon having no dispersion). The usual assumption that, since muons are lighter than nuclei, muon ZPM is fully adiabatically decoupled from the lattice [yielding 3 highest-frequency normal modes  $\omega_j$  describing single-particle muon ZPM; see Fig. 2(c)], corresponds to the weakly-bound (zero entanglement) adiabatic limit described above, but with the additional constraint of a harmonic  $V_{\text{eff}}$ . For  $\alpha\text{-N}_2$  this gives ZPE =  $0.58 \text{ eV}$  with contributions  $\text{ZPE}_j = \hbar\omega_j/2 = 0.17$  and  $0.20 \text{ eV}$ , and ZPM delocalization  $\Delta x_j = \sqrt{\hbar/(2m_\mu\omega_j)} = 0.23$  and  $0.21 \text{ \AA}$ , along the  $j = \text{L}$  and  $\text{T}_{1,2}$  directions, respectively [Fig. 2(a,b)]. The  $>40\%$  discrepancy between harmonic and anharmonic weakly-bound adiabatic values of  $\Delta x_{\text{L}}$  hints at the breakdown of the harmonic approximation due to strong anharmonicity [Fig. 2(a)].

Although the weakly-bound adiabatic limit is exact if  $m_\mu \rightarrow 0$ , it cannot reproduce muon–nuclear entanglement. In fact, in  $\alpha\text{-N}_2$  we see strong hybridization of the L muon normal mode with intra-molecular vibrations of both  $\text{N}_2$  in the  $[\text{N}_2\text{-}\mu\text{-N}_2]^+$  complex due to a finite muon mass [Fig. 2(c)], which implies significant muon–nuclear entanglement [39, 40]. This is detected by summing the muon motion amplitude squared over the top 3 (normalized) phonon normal modes and subtracting the weakly-bound (zero entanglement) value of 3, giving  $w_1 = -0.14 < 0$ . This defines an entanglement witness [23–25] as  $w_1 = 0$  for zero muon–nuclear entanglement and  $w_1 < 0$  in the entangled, many-body case. This again suggests that the weakly- (and possibly the strongly-) bound adiabatic approximation should fail, as muon–nuclear ZPM is inherently many-body, at least in the harmonic approximation. Were it not for strong anharmonicity, which invalidates the approach, such complex ZPM could still be treated by the full, many-body harmonic method by considering the entire supercell  $\Gamma$ -point phonon spectrum.

Finally, we turn to numerically-exact PIMD for calculating observables from arbitrary muon–nuclear ZPM [1–3], based on discretizing imaginary-time,  $T > 0$ , path integrals. Unlike approximate methods, PIMD works even in the anharmonic many-body regime with partial muon–nuclear entanglement [41]. Using PIMD we find [29] that the projected muon probability density is unimodal in  $\alpha\text{-N}_2$  [Fig. 2(a,b)], confirming that the muon site is unique even for quantum muons [33], with no signs of quantum tunneling. ZPM delocalization is  $\Delta x_j = 0.13$ ,  $0.15$ , and  $0.14 \text{ \AA}$  along the L,  $\text{T}_1$ , and  $\text{T}_2$  directions, respectively. Here  $\Delta x_{\text{L}}$  is large enough that anharmonic effects become significant [Fig. 2(a)] and harmonic approximations fail. Furthermore, all  $\Delta x_j$  are significantly smaller than in the weakly- and significantly larger than in the strongly-bound adiabatic approximation, implying partial muon–nuclear entanglement and many-body ZPM outside the scope of single-particle approximations, as anticipated [Fig. 2(c)]. To quantify the degree of entanglement we calculate a multivariate Pearson correlation coefficient [42]  $c_i = \langle \delta \mathbf{x}' \cdot \delta \mathbf{r}'_{\text{N}_i} \rangle / \sqrt{\langle |\delta \mathbf{x}'|^2 \rangle \langle |\delta \mathbf{r}'_{\text{N}_i}|^2 \rangle} \in [-1, 1]$ , between the centered muon displacement  $\delta \mathbf{x}' = \delta \mathbf{x} - \langle \delta \mathbf{x} \rangle$  and the centered displacement  $\delta \mathbf{r}'_{\text{N}_i} = \delta \mathbf{r}_{\text{N}_i} - \langle \delta \mathbf{r}_{\text{N}_i} \rangle$  of a nucleus  $i$ , via PIMD.  $w_{2i} = -|c_i| \in [-1, 0]$  is a witness of muon–nuclear entanglement [23–25] since  $w_{2i} = 0$  for separable (weakly-bound) states (as then  $\langle \delta \mathbf{x}' \cdot \delta \mathbf{r}'_{\text{N}_i} \rangle = \langle \delta \mathbf{x}' \rangle \cdot \langle \delta \mathbf{r}'_{\text{N}_i} \rangle = 0$ ) meaning that  $w_{2i} < 0$  implies entanglement. On the other hand, in the strongly-bound case (maximal entanglement) with  $\delta \tilde{\mathbf{r}}_{\text{N}_i} \propto \delta \mathbf{x}$  we find  $|c_i| = 100\%$ . In  $\alpha\text{-N}_2$  the degree of muon–nuclear entanglement is  $c_i \approx 55\%$  with the two nearest nitrogen, and decays with distance [Fig. 1(c)]. This confirms that muon–nuclear ZPM in  $\alpha\text{-N}_2$  is partially entangled and thus inherently many-body.

Detailed knowledge of the many-body muon–nuclear

Table I. Static NQCC  $C_Q^0$  of  $^{14}\text{N}$  in  $\alpha\text{-N}_2$  from uncalibrated DFT calculations, and calculations calibrated by  $f_{\text{cal}}$  obtained from fits of experimental QLCR spectra with predictions for a classical (DFT) or a quantum muon (PIMD; Fig. 3). Discrepancy from literature value  $-5.39(5)$  MHz [28] is given in standard deviations  $\sigma$ .

Calibration	$T$ (K)	$f_{\text{cal}}$	$C_Q^0$ (MHz)	Discrepancy ( $\sigma$ )
None		1	-5.76	-7.4(2)
Classical $\mu^+$	1.8	1.106(7)	-5.21(3)	3.1(6)
	5	1.103(4)	-5.22(2)	3.2(7)
Quantum $\mu^+$	1.8	1.076(6)	-5.35(3)	0.7(1)
	5	1.073(4)	-5.37(2)	0.4(1)

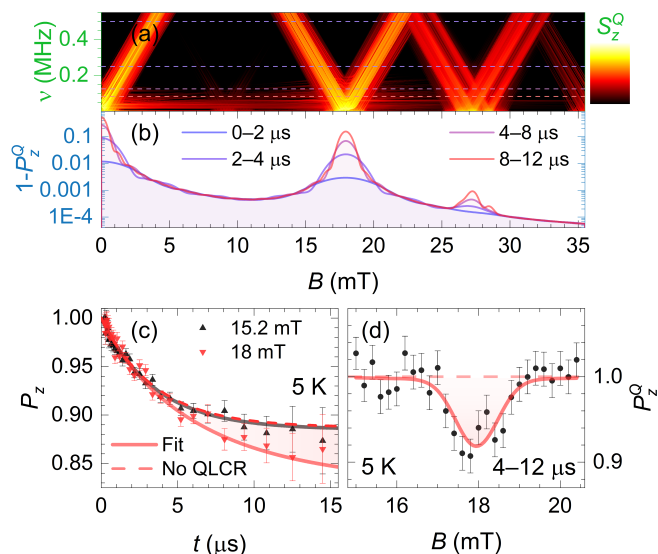


Figure 3. (a) Calibrated Fourier-transformed QLCR spectra  $S_z^Q(\nu, B)$  vs. frequency  $\nu$  from PIMD with 24 beads [29] for time-differential QLCR analysis [43]. (b) Muon-lifetime weighted integrals of  $1 - P_z^Q(t, B)$  over different time windows for integral QLCR analysis. (c) Experimental QLCR data at 5 K on (18 mT) and off resonance (15.2 mT) and the global fit with (solid) and without the QLCR term (dashed). (d) Global fit of 5 K QLCR data with PIMD predictions integrated over a 4–12  $\mu\text{s}$  time window vs.  $B$ .

ZPM afforded by PIMD allows us to derive an important constant: the static NQCC of  $^{14}\text{N}$  in  $\alpha\text{-N}_2$ , defined as  $C_Q^0 = e_0^2 q_0 Q / h$ , where  $Q = 2.044(3) \text{ fm}^2$  is the quadrupolar moment of  $^{14}\text{N}$  [31, 44], and  $q_0$  is the largest electric field gradient (EFG) tensor eigenvalue at  $^{14}\text{N}$ , assuming static classical nitrogen nuclei. The experimental NQCC  $C_Q = f(0)C_Q^0$  at  $T = 0$  is reduced from the static  $C_Q^0$  by the order parameter  $f(0) = 0.863(8) < 1$  due to the ZPM of nitrogen nuclei [28]. Using DFT we calculate  $C_Q^0$  by assuming classical point-nuclei in pristine  $\alpha\text{-N}_2$ , obtaining the *ab initio* value  $C_Q^{0,\text{DFT}} = -5.76$  MHz,

which differs from the accepted experimental value  $C_Q^0 = -5.39(5)$  MHz by  $\approx 6.9\%$  or  $\approx 7.4$  standard deviations  $\sigma$  (Table I). The discrepancy arises from systematic errors in DFT calculations of EFGs, which are apparently overestimated by a factor  $f_{\text{cal}} = C_Q^{0,\text{DFT}} / C_Q^0 \approx 1.07(1)$ . To obtain an independent estimate of  $C_Q^0 = f_{\text{cal}}^{-1} C_Q^{0,\text{DFT}}$  we must therefore determine  $f_{\text{cal}}$ , and calibrate the *ab initio* results against experiment.

We performed QLCR  $\mu\text{SR}$  experiments on  $\alpha\text{-N}_2$  on the EMU beamline [45] (ISIS pulsed muon source), using a custom-built TiZr gas condensation cell. A 100  $\mu\text{m}$  thick Ti window allowed surface muons to enter the sample volume, while a separate experiment confirmed negligible muon depolarisation in TiZr over the studied  $T$ . A  $^4\text{He}$  exchange gas cryostat around the cell provided control over sample  $T$  down to  $\sim 1.5$  K, while a 1/8" capillary connecting the cell to an external gas supply was heated along its length to avoid blockages. The sample was condensed from high purity (Grade 6.0)  $\text{N}_2$  gas, with  $\approx 1.8$  bar/l of gas being condensed at  $\approx 65$  K to ensure the  $\approx 1.6 \text{ cm}^3$  sample volume was full. Gas pressure was maintained well above the  $\text{N}_2$  triple point ( $\approx 0.125$  bar) throughout sample condensation to avoid deposition of the gas directly into the solid phase. Once condensation was complete, the sample was cooled through the freezing point at  $\approx 0.6$  K/min, with measurements confirming the sample was frozen.

In a QLCR experiment muons stops near  $I \geq 1$  nuclei (here  $^{14}\text{N}$ ), while a longitudinal magnetic field  $B$  is swept in small steps at a given  $T$  and the muon polarization  $P_z(t)$  is measured. For  $B$  where the Zeeman splitting of muon spin energy levels approaches the splitting of nuclear levels due to EFGs at nuclear positions, resonant cross-relaxation of muon–nuclear spins occurs, resulting in a sharp dip of late-time  $P_z(t)$  [27, 43, 46]. If we also have a good description of muon–nuclear ZPM (e.g., via PIMD), which shifts and reshapes QLCR spectra  $P_z(t, B)$ , we can extract muonated-sample EFGs and compare them to *ab initio* predictions to find the sought after factor  $f_{\text{cal}}$ . Since our modeling showed strongly time-window-dependent widths of QLCR spectral peaks in  $\alpha\text{-N}_2$  [Fig. 3(b)], we went beyond conventional QLCR analysis [43], and performed a simultaneous fit over all measured  $B$  and  $t < 18 \mu\text{s}$  (no binning with a 16 ns time resolution), at each measured  $T$ , using a simple global model  $P_z(t, B) = A_Q P_z^Q(t, B) + A_{\text{Mu}} e^{-\lambda_{\text{Mu}} t} + A_{\text{bgd}}(B)$ , where  $A_Q$  is the amplitude of QLCR signal,  $P_z^Q$  is the *ab initio* simulated QLCR signal (for either the classical or quantum case) at a given  $f_{\text{cal}}$  [Fig. 3(a,b)] [29],  $A_{\text{Mu}}$  describes the muonium fraction, known to form in  $\alpha\text{-N}_2$  [37] and relaxing with rate  $\lambda_{\text{Mu}}$ . The contribution  $A_{\text{bgd}}(B)$  due to muons stopped outside the sample was modeled as a constant plus a weak Lorentzian of  $B$ , with fits yielding a field variation of  $< 10\%$  of the QLCR signal [Fig. 3(c)], which does not affect our conclusions. These

fits described >28,000 experimental data points at each  $T$  using only 8 global parameters [Fig. 3(c,d)], with good fit quality [47] and without systematic deviations at any  $t$  or  $B$  [29]. This held true for both classical and quantum cases, as the main effect of muon–nuclear ZPM was a simple shift of the main QLCR peak, which was absorbed into the fitted value of  $f_{\text{cal}}$ . Extracting  $f_{\text{cal}}$  from QLCR spectra fits under the classical muon ansatz we thus obtain  $C_Q^0 = f_{\text{cal}}^{-1} C_Q^{0,\text{DFT}} = -5.22(2)$  MHz, which still differs from the accepted experimental value by  $\approx 3.2\sigma$  (Table I). However, extracting  $f_{\text{cal}}$  from QLCR spectra fits using a PIMD description of muon–nuclear ZPM, we obtain excellent agreement with previous experiments, with the final value  $C_Q^0 = -5.36(2)$  MHz (Table I) statistically even significantly more accurate than the previous best estimate  $-5.39(5)$  MHz [28].

In conclusion, we have performed an analysis of muon–nuclear ZPM in  $\alpha\text{-N}_2$ , culminating in a precision determination of the static NQCC of  $^{14}\text{N}$  in pristine  $\alpha\text{-N}_2$  using complementary QLCR experiments and state-of-the-art *ab initio* DFT+PIMD calculations, significantly improving the accuracy of this constant over the previous best value. We also discovered an electric-dipole polaron with strong effective mass renormalization around muons in  $\alpha\text{-N}_2$ , which might also affect the interpretation of experiments purportedly showing quantum muon tunneling in solid nitrogen [12]. More broadly, our work demonstrates the need to consider quantum effects when interpreting  $\mu\text{SR}$  data, paying attention to the presence of muon–nuclear entanglement or anharmonicity, to guide the choice of the applicable ZPM approximation.

Part of this work was performed at the STFC-ISIS facility. Computing resources were provided by the STFC Scientific Computing Department’s SCARF cluster and the Durham HPC Hamilton cluster. M.G., T.L., S.J.C., and F.L.P. are grateful to EPSRC (UK) for financial support through Grants No. EP/N024028/1 and EP/N024486/1. M.G. is grateful to the Slovenian Research Agency for financial support through Projects No. Z1-1852 and J1-2461. Research data from this paper will be made available via doi:xxx.

- 
- [1] C. P. Herrero and R. Ramirez, Path-integral simulation of solids, *J. Phys. Condens. Matter.* **26**, 233201 (2014).
- [2] M. Ceriotti, W. Fang, P. G. Kusalik, R. H. McKenzie, A. Michaelides, M. A. Morales, and T. E. Markland, Nuclear quantum effects in water and aqueous systems: Experiment, theory, and current challenges, *Chem. Rev.* **116**, 7529 (2016).
- [3] T. E. Markland and M. Ceriotti, Nuclear quantum effects enter the mainstream, *Nat. Rev. Chem.* **2**, 1 (2018).
- [4] S. J. Blundell, Spin-polarized muons in condensed matter physics, *Contemp. Phys.* **40**, 175 (1999).
- [5] S. J. Blundell, R. De Renzi, T. Lancaster, and F. L. Pratt, *Muon Spectroscopy: An Introduction* (Oxford University Press, Oxford, 2021).
- [6] A. Yaouanc and P. D. De Réotier, *Muon spin rotation, relaxation, and resonance: applications to condensed matter* (Oxford University Press, Oxford, 2011).
- [7] J. S. Möller, P. Bonfà, D. Ceresoli, F. Bernardini, S. J. Blundell, T. Lancaster, R. D. Renzi, N. Marzari, I. Watanabe, S. Sulaiman, and M. I. Mohamed-Ibrahim, Playing quantum hide-and-seek with the muon: localizing muon stopping sites, *Phys. Scr.* **88**, 068510 (2013).
- [8] P. Bonfà and R. De Renzi, Toward the computational prediction of muon sites and interaction parameters, *J. Phys. Soc. Jpn.* **85**, 091014 (2016), <https://doi.org/10.7566/JPSJ.85.091014>.
- [9] B. M. Huddart, *Muon stopping sites in magnetic systems from density functional theory*, Ph.D. thesis, Durham University (2020).
- [10] S. Mañas-Valero, B. M. Huddart, T. Lancaster, E. Coronado, and F. L. Pratt, Quantum phases and spin liquid properties of 1T-TaS<sub>2</sub>, *npj Quantum Mater.* **6**, 1 (2021).
- [11] G. Prando, P. Bonfà, G. Profeta, R. Khasanov, F. Bernardini, M. Mazzani, E. M. Brüning, A. Pal, V. P. S. Awana, H.-J. Grafe, B. Büchner, R. De Renzi, P. Carretta, and S. Sanna, Common effect of chemical and external pressures on the magnetic properties of RCoPO ( $R = \text{La, Pr}$ ), *Phys. Rev. B* **87**, 064401 (2013).
- [12] V. G. Storchak and N. V. Prokof’ev, Quantum diffusion of muons and muonium atoms in solids, *Rev. Mod. Phys.* **70**, 929 (1998).
- [13] C. P. Herrero and R. Ramírez, Diffusion of muonium and hydrogen in diamond, *Phys. Rev. Lett.* **99**, 205504 (2007).
- [14] B. M. Huddart, A. Hernández-Melián, T. J. Hicken, M. Gomilšek, Z. Hawkhead, S. J. Clark, F. L. Pratt, and T. Lancaster, MuFinder: A program to determine and analyse muon stopping sites, arXiv preprint (2021), [arXiv:2110.07341](https://arxiv.org/abs/2110.07341) [cond-mat.str-el].
- [15] A. V. Soudackov and S. Hammes-Schiffer, Removal of the double adiabatic approximation for proton-coupled electron transfer reactions in solution, *Chem. Phys. Lett.* **299**, 503 (1999).
- [16] A. R. Porter, M. D. Towler, and R. J. Needs, Muonium as a hydrogen analogue in silicon and germanium: Quantum effects and hyperfine parameters, *Phys. Rev. B* **60**, 13534 (1999).
- [17] P. Bonfà, F. Sartori, and R. De Renzi, Efficient and reliable strategy for identifying muon sites based on the double adiabatic approximation, *J. Phys. Chem. C* **119**, 4278 (2015).
- [18] I. J. Onuorah, P. Bonfà, R. De Renzi, L. Monacelli, F. Mauri, M. Calandra, and I. Errea, Quantum effects in muon spin spectroscopy within the stochastic self-consistent harmonic approximation, *Phys. Rev. Materials* **3**, 073804 (2019).
- [19] L. Monacelli, R. Bianco, M. Cherubini, M. Calandra, I. Errea, and F. Mauri, The stochastic self-consistent harmonic approximation: calculating vibrational properties of materials with full quantum and anharmonic effects, *J. Phys. Condens. Matter.* **33**, 363001 (2021).
- [20] M. A. Boxwell, T. A. Claxton, and S. F. J. Cox, *Ab initio* calculations on the hyperfine isotope effect between C<sub>60</sub>H and C<sub>60</sub>Mu, *J. Chem. Soc., Faraday Trans.* **89**, 2957 (1993).
- [21] J. S. Möller, D. Ceresoli, T. Lancaster, N. Marzari, and S. J. Blundell, Quantum states of muons in fluorides,

- Phys. Rev. B* **87**, 121108(R) (2013).
- [22] K. Yamada, Y. Kawashima, and M. Tachikawa, Accurate prediction of hyperfine coupling constants in muoniated and hydrogenated ethyl radicals: *ab initio* path integral simulation study with density functional theory method, *J. Chem. Theory Comput.* **10**, 2005 (2014).
- [23] M. B. Plenio and S. Virmani, An introduction to entanglement measures, *Quantum Info. Comput.* **7**, 1–51 (2007).
- [24] R. Horodecki, P. Horodecki, M. Horodecki, and K. Horodecki, Quantum entanglement, *Rev. Mod. Phys.* **81**, 865 (2009).
- [25] R. Horodecki, Quantum information, *Acta Phys. Pol.* **139**, 197 (2021).
- [26] T. A. Claxton, Muon-nuclear quadrupolar level crossing resonance in solid nitrogen. Evidence for  $[\text{N}_2\text{MuN}_2]^+$  complex formation?, *Philos. Mag. B* **72**, 251 (1995).
- [27] A. Abragam, Spectrométrie par croisements de niveaux en physique du muon, *C. R. Acad. Sci. Ser. B* **229**, 95 (1984).
- [28] T. A. Scott, Solid and liquid nitrogen, *Phys. Rep.* **27**, 89 (1976).
- [29] See Supplemental Material at [URL will be inserted by publisher] for details on DFT, MD, PIMD, and QLCR calculations. This material includes Refs. [5, 9, 14, 27, 28, 30, 31, 39, 40, 43, 44, 46, 48–57].
- [30] A. Erba, L. Maschio, S. Salustro, and S. Casassa, A post-Hartree–Fock study of pressure-induced phase transitions in solid nitrogen: The case of the  $\alpha$ ,  $\gamma$ , and  $\varepsilon$  low-pressure phases, *J. Chem. Phys.* **134**, 074502 (2011).
- [31] J. Rumble, *CRC Handbook of Chemistry and Physics*, 102nd ed. (CRC Press/Taylor & Francis Group, Boca Raton, 2021).
- [32] P. Botschwina, T. Dutoi, M. Mladenović, R. Oswald, S. Schmatz, and H. Stoll, Theoretical investigations of proton-bound cluster ions, *Faraday Discuss.* **118**, 433 (2001).
- [33] K. Terrill and D. J. Nesbitt, *Ab initio* anharmonic vibrational frequency predictions for linear proton-bound complexes  $\text{OC-H}^+-\text{CO}$  and  $\text{N}_2-\text{H}^+-\text{N}_2$ , *Phys. Chem. Chem. Phys.* **12**, 8311 (2010).
- [34] Q. Yu, J. M. Bowman, R. C. Fortenberry, J. S. Mancini, T. J. Lee, T. D. Crawford, W. Klemperer, and J. S. Francisco, Structure, anharmonic vibrational frequencies, and intensities of  $\text{NNHNN}^+$ , *J. Phys. Chem. A* **119**, 11623 (2015).
- [35] H.-Y. Liao, M. Tsuge, J. A. Tan, J.-L. Kuo, and Y.-P. Lee, Infrared spectra and anharmonic coupling of proton-bound nitrogen dimers  $\text{N}_2-\text{H}^+-\text{N}_2$ ,  $\text{N}_2-\text{D}^+-\text{N}_2$ , and  $^{15}\text{N}_2-\text{H}^+-^{15}\text{N}_2$  in solid para-hydrogen, *Phys. Chem. Chem. Phys.* **19**, 20484 (2017).
- [36] R. Hooper, D. Boutwell, and M. Kaledin, Assignment of infrared-active combination bands in the vibrational spectra of protonated molecular clusters using driven classical trajectories: Application to  $\text{N}_4\text{H}^+$  and  $\text{N}_4\text{D}^+$ , *J. Phys. Chem. A* **123**, 5613 (2019).
- [37] V. Storchak, J. H. Brewer, G. D. Morris, D. J. Arseneau, and M. Senba, Muonium formation via electron transport in solid nitrogen, *Phys. Rev. B* **59**, 10559 (1999).
- [38] M. H. Dehn, J. K. Shenton, S. Hohenstein, Q. N. Meier, D. J. Arseneau, D. L. Cortie, B. Hitti, A. C. Y. Fang, W. A. MacFarlane, R. M. L. McFadden, G. D. Morris, Z. Salman, H. Luetkens, N. A. Spaldin, M. Fechner, and R. F. Kiefl, Observation of a charge-neutral muon-polaron complex in antiferromagnetic  $\text{Cr}_2\text{O}_3$ , *Phys. Rev. X* **10**, 011036 (2020).
- [39] G. P. Srivastava, *The Physics of Phonons* (A. Hilger, Bristol Philadelphia, 1990).
- [40] L. Kantorovich, *Quantum Theory of the Solid State: An Introduction* (Kluwer Academic Publishers, Dordrecht Boston, 2004).
- [41] M. Shiga, Path integral simulations, in *Reference Module in Chemistry, Molecular Sciences and Chemical Engineering* (Elsevier, 2018).
- [42] T. Ichiye and M. Karplus, Collective motions in proteins: A covariance analysis of atomic fluctuations in molecular dynamics and normal mode simulations, *Proteins* **11**, 205 (1991).
- [43] J. S. Lord, F. L. Pratt, and M. T. F. Telling, Time differential ALC – experiments, simulations and benefits, *J. Phys. Conf. Ser.* **551**, 012058 (2014).
- [44] M. Tokman, D. Sundholm, P. Pyykkö, and J. Olsen, The nuclear quadrupole moment of  $^{14}\text{N}$  obtained from finite-element MCHF calculations on  $\text{N}^{2+}$  ( $2p$ ;  $^2\text{P}_{3/2}$ ) and  $\text{N}^+$  ( $2p^2$ ;  $^3\text{P}_2$  and  $2p^2$ ;  $^1\text{D}_2$ ), *Chem. Phys. Lett.* **265**, 60 (1997).
- [45] S. Giblin, S. Cottrell, P. King, S. Tomlinson, S. Jago, L. Randall, M. Roberts, J. Norris, S. Howarth, Q. Mutamba, N. Rhodes, and F. Akeroyd, Optimising a muon spectrometer for measurements at the ISIS pulsed muon source, *Nucl. Instrum. Methods Phys. Res. A* **751**, 70 (2014).
- [46] V. Storchak, G. Morris, K. Chow, W. Hardy, J. Brewer, S. Kreitzman, M. Senba, J. Schneider, and P. Mendels, Muon–nuclear quadrupolar level crossing resonance in solid nitrogen. Evidence for  $\text{N}_2\mu^+$  ion formation, *Chem. Phys. Lett.* **200**, 546 (1992).
- [47] The total global fit quality was  $\chi^2/\text{DOF} = 1.06$  and  $1.08$  at  $T = 1.8$  and  $5\text{K}$ , respectively.
- [48] S. J. Clark, M. D. Segall, C. J. Pickard, P. J. Hasnip, M. J. Probert, K. Refson, and M. Payne, First principles methods using CASTEP, *Z. Kristall.* **220**, 567 (2005).
- [49] J. P. Perdew, K. Burke, and M. Ernzerhof, Generalized gradient approximation made simple, *Phys. Rev. Lett.* **77**, 3865 (1996).
- [50] H. J. Monkhorst and J. D. Pack, Special points for Brillouin-zone integrations, *Phys. Rev. B* **13**, 5188 (1976).
- [51] A. Tkatchenko and M. Scheffler, Accurate molecular Van Der Waals interactions from ground-state electron density and free-atom reference data, *Phys. Rev. Lett.* **102**, 073005 (2009).
- [52] H. E. Maynard-Casely, J. R. Hester, and H. E. A. Brand, Re-examining the crystal structure behaviour of nitrogen and methane, *IUCrJ* **7**, 844 (2020).
- [53] S. E. Ashbrook and M. J. Duer, Structural information from quadrupolar nuclei in solid state NMR, *Concepts Magn. Reson. Part A Bridg. Educ. Res.* **28A**, 183 (2006).
- [54] C. Slichter, *Principles of Magnetic Resonance* (Springer-Verlag, Berlin New York, 1990).
- [55] F. L. Pratt, <http://shadow.nd.rl.ac.uk/calcalc/>, accessed: 2021-09-17.
- [56] J. Lord, S. Cottrell, and W. Williams, Muon spin relaxation in strongly coupled systems, *Physica B Condens. Matter* **289–290**, 495 (2000).
- [57] P. Zyla *et al.* (Particle Data Group), Review of Particle Physics, *Prog. Theor. Exp. Phys.* **2020**, 083C01 (2020).

# Supplemental Material: Many-Body Quantum Muon Effects and Quadrupolar Coupling in Solid Nitrogen

M. Gomilšek,<sup>1,2,3</sup> F. L. Pratt,<sup>4</sup> S. P. Cottrell,<sup>4</sup> S. J. Clark,<sup>3</sup> and T. Lancaster<sup>3</sup>

<sup>1</sup>*Jožef Stefan Institute, Jamova c. 39, SI-1000 Ljubljana, Slovenia*

<sup>2</sup>*Faculty of Mathematics and Physics, University of Ljubljana, Jadranska u. 19, SI-1000 Ljubljana, Slovenia*

<sup>3</sup>*Department of Physics, Durham University, South Road, Durham DH1 3LE, United Kingdom*

<sup>4</sup>*ISIS Muon Group, Science and Technology Facilities Council (STFC), Didcot OX11 0QX, United Kingdom*

(Dated: February 15, 2022)

## DFT CALCULATIONS

Both the pristine and muonated low- $T$  low-pressure  $\alpha$ -N<sub>2</sub> for short, was studied using the CASTEP plane-wave *ab initio* density functional theory (DFT) code [1] using the PBE exchange-correlation functional [2] and ultrasoft pseudopotentials. Calculations were carried out on a  $2 \times 2 \times 2$  supercell to avoid finite-size effects around the implanted muon, while a 1200 eV plane-wave energy cutoff and  $2 \times 2 \times 2$  Monkhorst-Pack grid [3] reciprocal-space sampling was chosen to achieve numerical convergence. All calculations were converged to within 0.1 eV in the self-consistent field (SCF) DFT loop, while geometry relaxation tasks were converged to within a tight  $0.5 \text{ meV } \text{\AA}^{-1}$  force tolerance on the muon and nuclei. Furthermore, to properly account for weak cohesive van der Waals (VdW) dispersion forces between N<sub>2</sub> molecules, which are usually underestimated in pure DFT, a Tkatchenko–Scheffler (TS) semi-empirical dispersion correction scheme was applied in a DFT-D approach [4]. We note, though, that the results of ordinary DFT with an *ad hoc* isotropic external hydrostatic pressure of 0.5 GPa (chosen to reproduce the experimental zero-pressure unit cell volume of pristine  $\alpha$ -N<sub>2</sub>) were practically indistinguishable from the results of full DFT-D calculations, even in the presence of an implanted muon. This indicates that in  $\alpha$ -N<sub>2</sub> the dominant VdW dispersion force contribution is a simple isotropic attraction among all nuclei and the muon.

Despite competing suggestions of a  $Pa\bar{3}$  (No. 205) or a  $P2_13$  (No. 198) cubic crystallographic structure of pristine  $\alpha$ -N<sub>2</sub> in the literature [5], we find that the higher-symmetry  $Pa\bar{3}$  structure is moderately preferred in our DFT calculations (by  $\sim 0.05$  eV per unit cell), in line with recent consensus [6–8]. In this structure the centers of N<sub>2</sub> molecules form a face-centered cubic (FCC) lattice [Fig. 1(a)].

## Classical muon stopping site

To find candidate muon stopping sites in  $\alpha$ -N<sub>2</sub> a muon’s initial position was randomly seeded in the unit cell and the full crystal geometry (including the muon position) relaxed at a fixed, experimental cell volume until

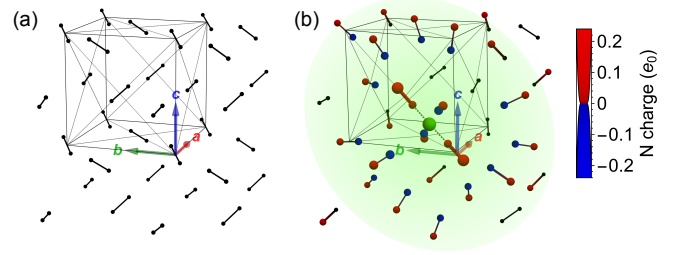


Figure 1. Alternative views of (a) the pristine  $\alpha$ -N<sub>2</sub> structure, where centers of N<sub>2</sub> molecules form an FCC lattice, and (b) the classical muon site where  $\mu^+$  (green) forms a linear  $[\text{N}_2-\mu-\text{N}_2]^+$  complex with two neighboring N<sub>2</sub> molecules at the center of an electric-dipole polaron (shading) [cf. Fig. 1(a,b) in the main text]. Induced Mulliken charge of nitrogen ions from DFT is represented by sphere size and color.

convergence. This process was repeated  $>20$  times to generate a list of candidate muon stopping sites, which were then grouped into clusters by identifying those candidate muon sites within  $<0.7 \text{ \AA}$  of each other (or of any in-between sites) as belonging to the same cluster. Here the distance between two arbitrary candidate muon sites  $\mathbf{r}_{\mu 1}$  and  $\mathbf{r}_{\mu 2}$  was taken as the minimal possible real-space distance  $|\mathbf{r}_{\mu 1} - T\mathbf{r}_{\mu 2}|$  under any symmetry operation  $T$  in the pristine  $\alpha$ -N<sub>2</sub> crystallographic space group  $Pa\bar{3}$  (including discrete translational, rotational and reflection symmetries). This is because the implanted muon is the sole source of local symmetry breaking in the crystal and thus muon sites related by pristine space-group symmetry operations should be regarded as identical. A muon site cluster can thus be thought of as a connected component in a graph whose vertices are the calculated muon sites that are considered adjacent if their minimal, symmetry-reduced distance is below a chosen threshold ( $0.7 \text{ \AA}$  in our case). We note that this symmetry-aware clustering algorithm based on graph theory is also implemented in the user-friendly MuFinder program for determining and analysing muon stopping sites [9, 10]. In the end, we find a single muon site cluster in  $\alpha$ -N<sub>2</sub>, which lies at the point midway between the centers of two neighboring N<sub>2</sub> molecules of the pristine  $\alpha$ -N<sub>2</sub> structure [Fig. 1(b)].

$\Gamma$ -point phonon spectra presented in the main text

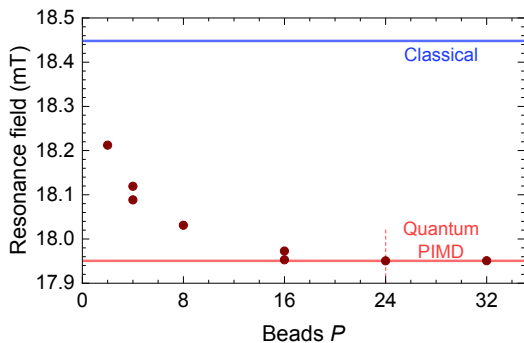


Figure 2. Convergence of PIMD calculations with the number of beads  $P$  as observed from the calibrated quadrupolar level-crossing resonance (QLCR) peak resonance field from a muon-lifetime weighed integral of the QLCR signal over a 4–8  $\mu$ s time window. The final number of beads  $P = 24$  for QLCR calculations presented in the main text is indicated by the dashed line.

were calculated on a  $2 \times 2 \times 2$  supercell of  $\alpha$ -N<sub>2</sub>, with whole isotope effect plot [Fig. 2(c) of the main text] generated from a single DFT calculation of phonon normal modes and frequencies. This was achieved by first reconstructing the dynamical matrix (DM) [11, 12], reweighting it by the desired muon isotope mass  $m_\mu$ , and then re-diagonalizing it to obtain the new phonon normal modes and frequencies.

### CLASSICAL MD AND QUANTUM PIMD CALCULATIONS

For PIMD calculations an NVT statistical ensemble of up to  $P = 32$  beads was simulated for up to  $S = 8600$  steps of 0.5 fs with a  $T = 20$  K stochastic Langevin thermostat. Satisfactory convergence in bead number was achieved already for  $P = 16$ –24 beads (Fig. 2). Classical MD simulations (which can be understood as a  $P = 1$  PIMD simulation) used the same statistical ensemble, time step, temperature, and thermostat and were run for up to  $S = 12000$  steps. Care was taken to ensure proper thermalization of the ensembles before observables were extracted from them.

Both PIMD and MD simulations produce a list of  $SP$  muon–nuclear configurations  $\{\mathbf{r}_i^{(s,p)}\}_{i=1}^K$ , where  $s = 1, \dots, S$  is the time step,  $p = 1, \dots, P$  is the bead index, and  $\mathbf{r}_i$  is the position of one muon or nucleus  $i$  out of  $K$  muons and nuclei present in the system. These muon–nuclear configurations follow the corresponding Boltzmann statistical probability distribution for finding muons and nuclei at these positions. In the case of MD this is the  $T > 0$  classical thermal probability distribution  $\rho_c(\mathbf{r}_1, \dots, \mathbf{r}_K)$ , while in PIMD this is the quantum thermal probability distribution  $\rho_q(\mathbf{r}_1, \dots, \mathbf{r}_K)$ , which at  $T = 0$  would coincide with the ground-state wave-

function’s  $|\psi\rangle$  probability distribution  $\rho_q(\mathbf{r}_1, \dots, \mathbf{r}_K) = |\psi(\mathbf{r}_1, \dots, \mathbf{r}_K)|^2$ . The thermal expectation value  $\langle O \rangle$  of any observable  $O$  that depends only on the muon–nuclear positions can thus be approximated from the numerical PIMD or MD samples by calculating the average

$$\langle O \rangle \approx \frac{1}{SP} \sum_{s=1}^S \sum_{p=1}^P O(\mathbf{r}_1^{(s,p)}, \dots, \mathbf{r}_K^{(s,p)}), \quad (1)$$

For observables that were expensive to calculate [e.g., the electric field gradients (EFG), which require a full DFT calculation for each muon–nuclear configuration in the average above] a further Monte Carlo approximation to the average was employed by randomly sampling only a small number of  $s$  and  $p$  ( $\approx 120$  in the case of EFGs) in Eq. (1).

### ZPM and quantum entanglement from PIMD

A numerical estimate of the average position  $\langle \mathbf{r}_i \rangle$  of a given muon or nucleus  $i$  can be calculated in this way by choosing  $O(\mathbf{r}_1, \dots, \mathbf{r}_K) = \mathbf{r}_i$  in Eq. (1). From this we can estimate the squared gyration radius  $\Delta r_i^2 = \langle |\delta \mathbf{r}_i|^2 \rangle = \langle |\mathbf{r}_i - \langle \mathbf{r}_i \rangle|^2 \rangle$ , which corresponds to choosing  $O = |\mathbf{r}_i - \langle \mathbf{r}_i \rangle|^2$ , and the covariance  $\langle \delta \mathbf{r}_i \cdot \delta \mathbf{r}_{i'} \rangle$  by choosing  $O = (\mathbf{r}_i - \langle \mathbf{r}_i \rangle) \cdot (\mathbf{r}_{i'} - \langle \mathbf{r}_{i'} \rangle)$ . Using these we can then extract a numerical estimate of the multivariate Pearson correlation coefficient  $c_{ii'} = \langle \delta \mathbf{r}_i \cdot \delta \mathbf{r}_{i'} \rangle / (\Delta r_i \Delta r_{i'}) \in [-1, 1]$  [13]. If this is non-zero as  $T \rightarrow 0$  it implies ground-state positional entanglement of muons or nuclei  $i$  and  $i'$  (see main text). We can also calculate the squared ZPM delocalization of a muon  $\Delta x_j^2$  along a given direction  $j = L, T_1, T_2$  (see main text), by choosing  $O = |(\Delta \mathbf{x} - \langle \Delta \mathbf{x} \rangle) \cdot \hat{\mathbf{v}}_j|^2$  for the corresponding unit vector  $\hat{\mathbf{v}}_j$  along this direction.

### Thermal effects and classical MD

Since PIMD calculations actually require a finite temperature for numerical convergence ( $T = 20$  K in our calculations) we also checked that the observed quantum effects were not masked by thermal excitations by comparing them against complementary classical MD simulations. We find that the pure thermal spread of muon–nuclear positions is indeed much smaller at  $\Delta x_j = 0.08$  and  $0.07$  Å along  $j = L$  and  $T_{1,2}$ , respectively, than the quantum widths (see main text), as can be expected from the steepness of the calculated effective potentials (Fig. 2 in the main text) in relation to the thermal equipartition energy  $k_B T/2 = 1.7$  meV at this  $T$ .

## CALCULATION OF QLCR SPECTRA

If we were to assume fixed classical muon–nuclear positions  $\{\mathbf{r}_i\}_{i=1}^K$  and the corresponding EFG tensors  $\{V_i\}_{i=1}^K$  at those positions (these can be calculated from the muon–nuclear positions using DFT), the muon and nuclear spins would interact via a Hamiltonian composed of a Zeeman contribution  $H_Z$ , a local quadrupolar contribution  $H_Q$ , and a dipole coupling contribution  $H_D$  [14–17]

$$\begin{aligned} H &= H_Z + H_Q + H_D, \\ H_Z &= - \sum_i \gamma_i \hbar \mathbf{S}_i \cdot \mathbf{B}, \\ H_Q &= \sum_i \frac{e_0 Q_i}{2S_i(2S_i - 1)} \mathbf{S}_i \cdot V_i \mathbf{S}_i, \\ H_D &= \sum_{\langle ii' \rangle} \frac{\mu_0 \gamma_i \gamma_{i'} \hbar^2}{4\pi |\mathbf{r}_{ii'}|^3} [\mathbf{S}_i \cdot \mathbf{S}_{i'} - 3(\mathbf{S}_i \cdot \hat{\mathbf{r}}_{ii'}) (\hat{\mathbf{r}}_{ii'} \cdot \mathbf{S}_{i'})], \end{aligned} \quad (2)$$

where  $\gamma_i$  is the gyromagnetic ratio of muon or nucleus  $i$  with spin vector  $\mathbf{S}_i$ , spin size  $S_i$ , and nuclear quadrupole moment  $Q_i$ ,  $\mathbf{B}$  is the applied magnetic field,  $e_0$  is the elementary charge,  $\mu_0$  is vacuum permeability, the sum in  $H_D$  is over unique pairs of muon or nuclei  $\langle ii' \rangle$ ,  $\mathbf{r}_{ii'} = \mathbf{r}_i - \mathbf{r}_{i'}$  is a vector from a muon or nucleus  $i'$  to  $i$ , and  $\hat{\mathbf{r}}_{ii'} = \mathbf{r}_{ii'} / |\mathbf{r}_{ii'}|$  is a unit vector in the same direction. However, due to both quantum ZPM and thermal movement the muons and nuclei in this Hamiltonian do not have fixed classical (point-particle) positions, nor are the EFGs independent of those positions.

To reduce the complexity of solving the coupled spin–positional Hamiltonian of Eq. (2), we assume that there is no significant entanglement between the spin and spatial degrees of freedom in the  $T \approx 0$  ground-state wavefunction of the system, i.e., that  $|\psi\rangle = |\psi\rangle_{\text{spin}} \otimes |\psi\rangle_{\text{position}}$ , due to a separation of timescales for positional and spin dynamics. In this way we can construct an effective spin-only Hamiltonian operator by averaging out the positional degrees of freedom with a partial trace

$$H_{\text{eff,spin}} = \text{tr}_{\text{position}} \{\rho H\}, \quad (3)$$

where  $\rho$  is the total density matrix, which at  $T = 0$  equals simply  $\rho = |\psi\rangle\langle\psi|$ ; i.e., at  $T = 0$  we have  $H_{\text{eff,spin}} = \text{position} \langle \psi | H | \psi \rangle_{\text{position}}$ . In PIMD and MD simulations this can be done by numerically calculating an average over positional degrees of freedom via Eq. (1) where the observable  $O$  is taken to be the Hamiltonian  $H$  from Eq. (2), and at each muon–nuclear configuration sample  $\{\mathbf{r}_i^{(s,p)}\}_{i=1}^K$  we recalculate the corresponding EFG tensors  $V_i$  via DFT. As mentioned previously, due to the time complexity of calculating the EFG tensors, the full Eq. (1) is approximated via Monte Carlo sampling of  $\approx 120$  random  $s$  and  $p$  indices from the PIMD or MD muon–nuclear configurations  $\{\mathbf{r}_i^{(s,p)}\}_{i=1}^K$ .

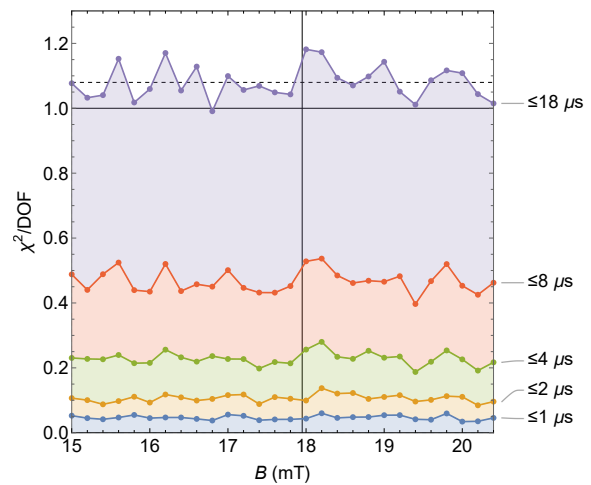


Figure 3. Field- and time-resolved quality of the global fits of QLCR spectra described in the main text at  $T = 5$  K. The contributions towards the total reduced  $\chi^2/\text{DOF}$  at each applied field  $B$  are shown cumulatively up to different times after muon implantation. The horizontal dashed line shows the average  $\chi^2/\text{DOF} = 1.08$  across all  $B$  (i.e., total  $\chi^2/\text{DOF}$  of the global fit), while the vertical line shows the main QLCR resonance field (Fig. 2).

The numerical calculation of a single Hamiltonian sample from the muon–nuclear configuration and the corresponding EFG tensors was performed using the CalcALC program [18] by considering only the four  $^{14}\text{N}$  nuclei in the  $[\text{N}_2-\mu-\text{N}_2]^+$  complex, i.e. the four nitrogen nuclei closest to the muon, since further-away nitrogen nuclei are only very weakly dipolarly coupled to the muon and thus do not affect its relaxation much. A  $^{14}\text{N}$  nuclear quadrupole moment of  $Q = 2.044(3) \text{ fm}^2$  was used [8, 19]. Once the effective spin-only Hamiltonian was thus calculated, a CalcALC-inspired Mathematica program was used to calculate the time-dependent muon relaxation signal  $P_z^Q(t)$  due to QLCR via exact diagonalization as in Ref. [20] for a range of applied magnetic fields  $B$ . At this stage, the quadrupolar contribution  $H_Q$  was multiplied by an EFG calibration factor  $f_{\text{cal}}^{-1} \approx 1$ , removing most of the otherwise unavoidable systematic errors of DFT, as explained in the main text. In global fits of experimental QLCR spectra described in the main text  $f_{\text{cal}}$  was adjusted in a loop until convergence to a minimal  $\chi^2$  was achieved. We note that in these fits no systematic deviations at any  $t$  or  $B$  were observed (Fig. 3).

The final, calibrated QLCR spectra  $1 - P_z^Q(t, B)$  exhibit a non-trivial dependence on time  $t$  and applied field  $B$  and are shown in Fig. 4. Their Fourier transforms

$$S_z^Q(\nu, B) = \frac{1}{2\pi} \int_{-\infty}^{\infty} [1 - P_z^Q(t, B)] e^{-\nu t} dt, \quad (4)$$

where  $\nu$  is the frequency, and their integrals over select

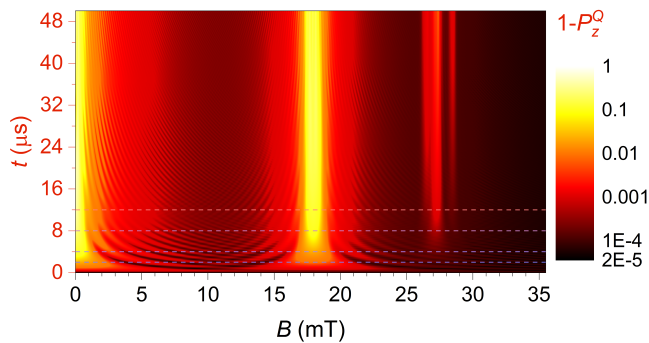


Figure 4. Calibrated QLCR spectra  $1 - P_z^Q(t, B)$  from PIMD with 24 beads for time-differential QLCR analysis [21]. Dashed lines indicate time windows boundaries for QLCR signal integrals shown in Fig. 3(b) in the main text.

time windows  $t \in [t_1, t_2]$

$$\overline{P}_z^Q(B) = \frac{\int_{t_1}^{t_2} P_z^Q(t, B) e^{-t/\tau_\mu} dt}{\int_{t_1}^{t_2} e^{-t/\tau_\mu} dt}, \quad (5)$$

weighed by the mean muon lifetime  $\tau_\mu = 2.197 \mu\text{s}$  [22] to account for the exponential decay of muons and their Poissonian counting statistics in  $\mu\text{SR}$  measurements [23], are shown in Fig. 3(a,b) in the main text.

- 
- [1] S. J. Clark, M. D. Segall, C. J. Pickard, P. J. Hasnip, M. J. Probert, K. Refson, and M. Payne, First principles methods using CASTEP, *Z. Kristall.* **220**, 567 (2005).
  - [2] J. P. Perdew, K. Burke, and M. Ernzerhof, Generalized gradient approximation made simple, *Phys. Rev. Lett.* **77**, 3865 (1996).
  - [3] H. J. Monkhorst and J. D. Pack, Special points for Brillouin-zone integrations, *Phys. Rev. B* **13**, 5188 (1976).
  - [4] A. Tkatchenko and M. Scheffler, Accurate molecular Van Der Waals interactions from ground-state electron density and free-atom reference data, *Phys. Rev. Lett.* **102**, 073005 (2009).
  - [5] T. A. Scott, Solid and liquid nitrogen, *Phys. Rep.* **27**, 89 (1976).
  - [6] A. Erba, L. Maschio, S. Salustro, and S. Casassa, A post-Hartree-Fock study of pressure-induced phase transitions in solid nitrogen: The case of the  $\alpha$ ,  $\gamma$ , and  $\epsilon$  low-pressure phases, *J. Chem. Phys.* **134**, 074502 (2011).
  - [7] H. E. Maynard-Casely, J. R. Hester, and H. E. A. Brand,

- Re-examining the crystal structure behaviour of nitrogen and methane, *IUCrJ* **7**, 844 (2020).
- [8] J. Rumble, *CRC Handbook of Chemistry and Physics*, 102nd ed. (CRC Press/Taylor & Francis Group, Boca Raton, 2021).
  - [9] B. M. Huddart, A. Hernández-Melián, T. J. Hicken, M. Gomilšek, Z. Hawkhead, S. J. Clark, F. L. Pratt, and T. Lancaster, MuFinder: A program to determine and analyse muon stopping sites, arXiv preprint (2021), arXiv:2110.07341 [cond-mat.str-el].
  - [10] B. M. Huddart, *Muon stopping sites in magnetic systems from density functional theory*, Ph.D. thesis, Durham University (2020).
  - [11] G. P. Srivastava, *The Physics of Phonons* (A. Hilger, Bristol Philadelphia, 1990).
  - [12] L. Kantorovich, *Quantum Theory of the Solid State: An Introduction* (Kluwer Academic Publishers, Dordrecht Boston, 2004).
  - [13] T. Ichiye and M. Karplus, Collective motions in proteins: A covariance analysis of atomic fluctuations in molecular dynamics and normal mode simulations, *Proteins* **11**, 205 (1991).
  - [14] A. Abragam, Spectrométrie par croisements de niveaux en physique du muon, *C. R. Acad. Sci. Ser. B* **229**, 95 (1984).
  - [15] V. Storchak, G. Morris, K. Chow, W. Hardy, J. Brewer, S. Kreitzman, M. Senba, J. Schneider, and P. Mendels, Muon—nuclear quadrupolar level crossing resonance in solid nitrogen. Evidence for  $\text{N}_2\mu^+$  ion formation, *Chem. Phys. Lett.* **200**, 546 (1992).
  - [16] S. E. Ashbrook and M. J. Duer, Structural information from quadrupolar nuclei in solid state NMR, *Concepts Magn. Reson. Part A Bridg. Educ. Res.* **28A**, 183 (2006).
  - [17] C. Slichter, *Principles of Magnetic Resonance* (Springer-Verlag, Berlin New York, 1990).
  - [18] F. L. Pratt, <http://shadow.nd.rl.ac.uk/calcalc/>, accessed: 2021-09-17.
  - [19] M. Tokman, D. Sundholm, P. Pyykkö, and J. Olsen, The nuclear quadrupole moment of  $^{14}\text{N}$  obtained from finite-element MCHF calculations on  $\text{N}^{2+}$  ( $2p$ ;  $^2P_{3/2}$ ) and  $\text{N}^+$  ( $2p^2$ ;  $^3P_2$  and  $2p^2$ ;  $^1D_2$ ), *Chem. Phys. Lett.* **265**, 60 (1997).
  - [20] J. Lord, S. Cottrell, and W. Williams, Muon spin relaxation in strongly coupled systems, *Physica B Condens. Matter* **289-290**, 495 (2000).
  - [21] J. S. Lord, F. L. Pratt, and M. T. F. Telling, Time differential ALC – experiments, simulations and benefits, *J. Phys. Conf. Ser.* **551**, 012058 (2014).
  - [22] P. Zyla *et al.* (Particle Data Group), Review of Particle Physics, *Prog. Theor. Exp. Phys.* **2020**, 083C01 (2020).
  - [23] S. J. Blundell, R. De Renzi, T. Lancaster, and F. L. Pratt, *Muon Spectroscopy: An Introduction* (Oxford University Press, Oxford, 2021).